EMAS
Engineering Modelling, Analysis & Simulation
THE NAFEMS JOURNAL

NAFEMS
Vol.3, Issue 1, 2026

Estimation of Wall Thickness in Middle Cerebral Artery Aneurysms Using Fluid-Structure Interaction Simulations

Jozsef Nagy[a], Wolfgang Fenz[b], Michael Giretzlehner[b], Vanessa Mazanec[c], Zoltan Major[d], Andreas Gruber[c,e], Philip-Rudolf Rauch [c,e,1], Philip Cardiff[f], Matthias Gmeiner[c,e]

[a]eulerian-solutions e.U., Leonfeldnerstrasse 245, 4040 Linz, Austria
[b]RISC Software GmbH, Softwarepark 32a, 4232 Hagenberg, Austria
[c]Department of Neurosurgery, Kepler University Hospital and Johannes Kepler University, Wagner-Jauregg-Weg 15, 4020 Linz, Austria
[d]Institute of Polymer Product Engineering, Johannes Kepler University Linz, Altenbergerstasse 69, 4040 Linz, Austria
[e]Clinical Research Institute for Neurosciences, Faculty of Medicine, Johannes Kepler University, Altenbergerstasse 69 4040 Linz, Austria
[f]University College Dublin, School of Mechanical and Materials Engineering, Belfield, D04 V1W8 Dublin, Ireland

Abstract

Patient-specific modeling of vessel wall thickness remains a key challenge in Fluid–Structure Interaction (FSI) simulations of cerebral aneurysms. To address this gap, the authors introduce the “aneurysm-OSI-band” (AOB)—derived from the Oscillatory Shear Index (OSI)—as a marker of localized wall thickness. Moreover, this study provides a direct comparison of OSI calculations against intraoperative imaging, offering confirmation of the AOB approach. In addition, FSI convergence is improved with an optimized residual method.

A total of 25 Middle Cerebral Artery (MCA) aneurysms treated at a single institution between 2016 and 2020 were retrospectively analyzed. Digital subtraction angiography (DSA) data were used for FSI simulations and OSI calculation. The resulting OSI maps were systematically compared with intraoperative images, wherein thin- and thick-walled regions were identified macroscopically. This correlation enabled statistical comparison and assessment of the accuracy of the AOB in localizing distinct wall-thickness profiles.

Defining the AOB based on OSI values revealed a statistically significant distinction between thin- and thick-walled aneurysm segments. Quantitative analysis demonstrated robust concordance between simulation-derived OSI patterns and intraoperative observations, highlighting OSI value differences between thin and thick-walled areas.

The introduction of the AOB provides a method for assessing patient-specific wall thickness and determining rupture status. These findings underscore the potential of advanced computational modeling to improve personalized aneurysm management and enhance clinical outcomes.

Keywords

Cerebral aneurysm, middle cerebral artery, wall thickness, intraoperative images, Fluid-Structure Interaction

---

[1] Corresponding author.

E-mail address: Philip-Rudolf.Rauch@kepleruniklinikum.at (Philip-Rudolf Rauch)

https://doi.org/10.59972/bkzfvrqx

1 Introduction

Cerebral aneurysms are estimated to occur in approximately 2–5% of the general population [1]. When such aneurysms rupture, leading to subarachnoid hemorrhage (SAH), the resulting morbidity and mortality are substantial. Numerous medical, genetic, morphological, and hemodynamic factors have been implicated in aneurysm formation, growth, and rupture [2–4]. Although treatment is recommended in selected cases, it carries inherent procedural risks that must be carefully balanced against rupture risk [5].

Patient-specific aneurysm simulations have emerged as a valuable tool for guiding the decision to treat, yet these simulations are hindered by limited data on patient-specific vessel wall thickness, necessitating often simplistic wall assumptions. Recent studies highlight the need for such predictive tools by correlating calcified or atherosclerotic plaque presence with elevated periprocedural complications [6–8]. Specifically, thick and rigid aneurysm walls can complicate simple clipping procedures through a heightened risk of parent artery occlusion or embolic events [6–8]. Conversely, thin-walled regions may rupture prematurely, increasing morbidity and mortality [9, 10]. By refining simulation-based analyses of aneurysm wall behavior, the proposed methodology endeavors to provide neurosurgeons with a framework for risk assessment and procedural planning.

Computational fluid dynamics (CFD) studies have attempted to address these challenges by focusing on wall shear stress (WSS) and the oscillatory shear index (OSI) to characterize thin- and thick-walled aneurysm regions [9,11–22]. However, results remain inconsistent: while Furukawa et al.8 have shown elevated OSI in regions with hyperplastic thick-walled remodeling, other studies report no significant differences [21–24]. Moreover, many CFD models do not fully account for the structural properties of the aneurysm wall. Fluid-structure interaction (FSI) approaches—by analyzing both blood flow and wall mechanics—offer a more holistic perspective [25, 26].

In this study, the authors integrate detailed structural property analyses into FSI simulations, enhancing existing predictive models of aneurysm wall thickness. In addition, an improved coupling method is introduced to reduce calculation cost for simulations. Within this framework, the “aneurysm-OSI-band” (AOB) is introduced as a novel hemodynamic metric that refines the stratification of aneurysm wall characteristics for future operative planning. By combining the AOB with structural mechanics, hemodynamics, and FSI, this work aims to deliver a more precise and clinically relevant assessment of diverse aneurysm wall properties, ultimately improving preoperative planning and clinical outcomes.

2 Methods

2.1 Patient data

A total of 25 Middle Cerebral Artery (MCA) aneurysms treated at the authors’ institution between 2016 and 2020 were initially evaluated. Intraoperative videos were available for these patients, allowing the extraction of still images to assess aneurysm wall thickness, as previously described in [8,27–29]. Intraoperative images were reviewed to classify wall thickness by identifying thin (red, translucent areas) and thick (white or yellow, often calcified) regions relative to adjacent healthy vessel tissue [8,27–29]. Fluid–structure interaction simulations were then conducted to compare these empirically observed wall-thickness distributions with computational predictions (see section wall thickness analysis).

For all patients in the overall cohort, the existence of an “Aneurysm-OSI-band” AOB was determined. Patient-specific parameters, including age, gender, arterial hypertension, smoking status, and alcohol use, were extracted retrospectively from medical records. Digital subtraction angiography (DSA) data were used for aneurysm segmentation, employing intensity thresholding followed by minor adjustments to the voxel volume. The segmented geometries were then exported as surface meshes in STL format. Inlet and outlet boundary planes were established, and a volumetric fluid mesh was automatically generated from these STL files. The solid vessel wall mesh was subsequently extruded from the fluid mesh at a uniform thickness of 0.2 mm, in accordance with values reported in the literature [25,30].

2.2 Hemodynamic and structural mechanical modeling

The computational fluid dynamics (CFD) tool OpenFOAM [31], in conjunction with an extended and improved version of the fluid-structure interaction (FSI) library solids4Foam [32-35], was used to numerically solve unsteady equations. Fluid dynamic (in medicine also called hemodynamic) modelling was based on the principles of mass and momentum conservation, employing the continuity equation and Navier-Stokes equations. These equation in differential form are defined by

$$\frac{\partial \rho}{\partial t} + \nabla \cdot (\rho \boldsymbol{u}) = 0, \tag{1}$$

$$\frac{\partial \rho \boldsymbol{u}}{\partial t} + \nabla \cdot (\rho\, \boldsymbol{u} \otimes \boldsymbol{u}) = -\nabla p + \nabla \cdot \tau + \boldsymbol{F}, \tag{2}$$

Here, ρ represents the fluid density, the vector $\boldsymbol{u}$ is the fluid velocity. p is the pressure, τ is the viscous stress tensor and $\mathbf{F}$ represents any additional force acting upon the fluid.

Inflow boundary conditions were defined by a pulsatile flow profile with a temporal velocity curve derived from published data [36]. Outflow conditions were time-dependent and based on experimental pressure measurements [37]. A no-slip condition was assumed along the interior vessel walls. Blood was modelled as a Newtonian fluid with a viscosity of 0.004 Pa*s and a density of 1060 kg/m³. Simulations were performed over one cardiac cycle (1 second) at 60 beats per minute, discretized into 100-time increments. For structural mechanics, vessel walls were fixed at the inflow and outflow points.

Structural mechanical modelling utilized the generalized version of Newton's second law. In the context of continuum mechanics, these principles are often expressed in integral form, which accounts for the distribution of forces and accelerations over the entire volume and surface of the structure.

$$\int_{\Omega_o} \rho_o \frac{\partial^2 \boldsymbol{D}}{\partial t^2} d\Omega_o = \oint_{\Gamma_o} \boldsymbol{n_o} \cdot \sigma_s \, d\Gamma_o + \int_{\Omega_o} \rho_o \boldsymbol{b} \; d\Omega_o, \tag{3}$$

In equation 3, Ω_o denotes the reference volume of the structure, acting as the domain for the integral equations. The density ρ_o represents the solid material's density. The displacement $\mathbf{D}$ illustrates how material points are displaced from their initial positions. The surface Γ_o encloses volume Ω_o, with $\boldsymbol{n_o}$ being the outward normal vector on this surface. The stress tensor σ_s describes the internal stresses within the material. $\mathbf{b}$ represents possible body forces, such as gravity, acting throughout the volume.

Equation 3 gives the partial differential equation describing a linear elastic material. The constitutive equation for such a linear elastic, isotropic material relating stress to strain is given by

$$\sigma_s = 2\mu\varepsilon_s + \lambda \, tr(\varepsilon_s) \, I, \tag{4}$$

In this equation, μ denotes the shear modulus and the term ε_s represents the strain tensor. Additionally, λ is the first Lamé parameter. The strain can be expressed in terms of the displacement fields as follows:

$$\varepsilon_s = \frac{1}{2}(\nabla \boldsymbol{D} + (\nabla \boldsymbol{D})^T), \tag{5}$$

Here, μ and λ can be related to Young's modulus E and Poisson's ratio ν through the following equations:

$$\mu = \frac{E}{2(1+\nu)}, \tag{6}$$

$$\lambda = \frac{\nu E}{(1+\nu)(1-2\nu)} \tag{7}$$

Vascular tissue properties were approximated using the presented linear elastic material behavior with a Young's modulus of 2.49 MPa [38] and a Poisson's ratio of 0.49 [25,39].

All aneurysms were analyzed with respect to selected morphological, hemodynamic and structural mechanical parameters, which included the most important quantities identified in literature (see Table 1).

2.3 Fluid-Structure Interaction coupling

Equations 1-3 were solved sequentially and coupled using an FSI boundary condition. This specific implementation utilizes the open-source library solids4Foam, which extends the capabilities of OpenFOAM for solid mechanics and FSI problems [27]. The method was fully validated against experimental data in a previous work [34]. In this segregated method, coupling occurs through the exchange of data across the shared FSI boundary. This approach, also known as a segregated method, stands in contrast to monolithic methods where all equations are solved simultaneously within a single system. An FSI iteration in a given time step is implemented as follows:

1. On the fluid side, the process starts by solving the governing equations (as described in equations 1-2) to obtain the velocity-pressure fields. The velocity-pressure coupling within the fluid solver is handled by the PIMPLE algorithm (see Figure 1.a), a robust method in OpenFOAM derived from the PISO algorithm.

2. From the velocity field the WSS and OSI distributions are calculated (see Figure 1.b).
3. Specific fluid quantities, such as pressure and viscous stresses, are interpolated onto the solid mesh at the FSI boundary (see Figure 1.b).
4. On the solid side, these forces act as boundary body forces in equation 3, producing a displacement field.
5. Important solid quantities such as the equivalent stress (MISES) and strain (ES) are calculated (see Figure 1.b).
6. The displacement is then interpolated back onto the fluid mesh, causing the fluid domain to deform accordingly. This mesh motion is managed using a Laplacian equation, which allows the computational grid to move in a continuous and smooth way.
7. As a result, the fluid equations need to be solved again to account for the mesh deformation.

This cycle 1-7 continues until convergence criteria are satisfied withing an FSI iteration. To enhance convergence speed and stability, Aitken underrelaxation is employed to dynamically adjust iteration parameters. Once a stable coupled solution is obtained for the current time step, the simulation advances to the next time step, and the cycle repeats.

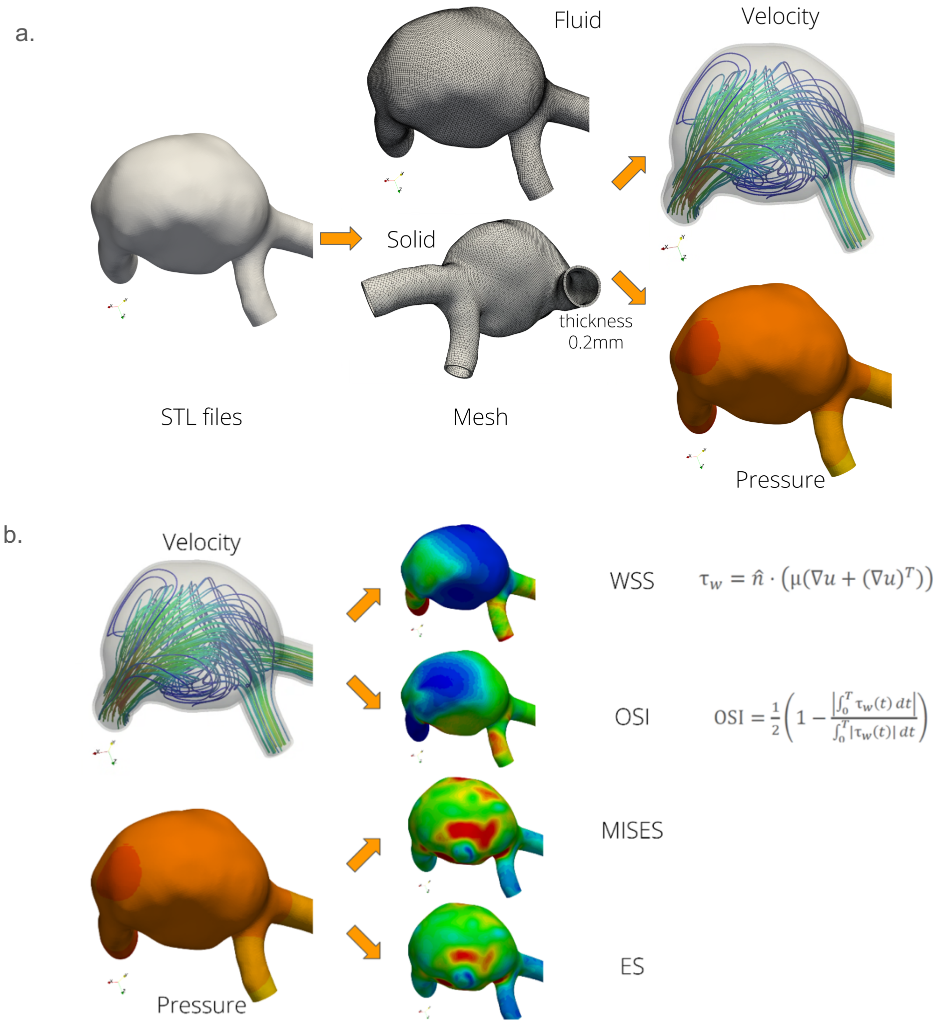

Figure 1. Schematic simulation workflow: Aneurysm geometry as STL, calculation grid, simulations results of velocity and pressure calculated with the PIMPLE algorithm (a); derivation of WSS and OSI from the velocity, pressure is utilized as body force in the solid equations influencing the wall stress as well as strain results.

In this study we introduce a novel residual approach in the solids4Foam framework and investigate the difference to the default residual approaches to improve FSI convergence within a given time step.

1. Residual method #1: Comparison of displacement increment (default method)

2. Residual method #2: Comparison of absolute node positions (novel improved method)

Residual method #1 is the default method in the FSI library solids4Foam [32-34] for convergence calculation. This method calculates the residual by directly comparing the change in displacement (the increment) of the fluid interface with the change in displacement of the solid interface for the current FSI iteration.

The residual at the i-th FSI iteration, $\mathbf{R}_\mathrm{i}$, on the FSI interface is defined as:

$$\boldsymbol{R}_i = \mathcal{M}_{s \to f}(\Delta \boldsymbol{d}_i^s) - \Delta \boldsymbol{d}_i^f \tag{8}$$

Here, $\Delta\mathbf{d}_\mathrm{i}^\mathrm{s}$ is the displacement increment of the solid interface calculated during iteration i and $\Delta\mathbf{d}_\mathrm{i}^\mathrm{f}$ is the displacement increment of the fluid interface during the same iteration i. $\mathcal{M}_{s \to f}(\dots)$ is a function for mapping structural node coordinates onto the fluid boundary mesh for direct comparison.

Residual method #2 calculates the residual $\mathbf{R}_\mathrm{i}$ by comparing the absolute spatial coordinates of the fluid and solid interfaces after the current FSI iteration. The position of the fluid interface is its position at the start of the time step t_n plus its displacement increment for the iteration i:

$$x_i^f = x(t_n)^f + \Delta \boldsymbol{d}_i^f \tag{9}$$

The position of the solid interface is calculated similarly:

$$x_i^s = x(t_n)^s + \Delta \boldsymbol{d}_i^s \tag{10}$$

The residual at the i-th FSI iteration $\mathbf{R}_\mathrm{i}$ is then the difference between the mapped solid position and the fluid position:

$$R_i = \mathcal{M}_{s \to f}(x_{\boldsymbol{i}}^{\boldsymbol{s}}) - x_{\boldsymbol{i}}^{\boldsymbol{f}} \tag{11}$$

Substituting the position definitions from equations 9 and 10, we get:

$$R_i = \mathcal{M}_{s \to f}(x(t_n)^s + \Delta d_i^s) - \left(x(t_n)^f + \Delta d_i^f\right) \tag{12}$$

For both methods, convergence is achieved when R_i approaches 0 with a user defined tolerance (in this work 1e-4). In this case, equation 12 reduces to equation 8 and both residual approaches deliver identical results.

2.4 Aneurysm-OSI-band

Figure 2.a and b. illustrate the newly defined hemodynamic phenomenon referred to as the “aneurysm-OSI-band” (AOB). This phenomenon is characterized by three specific criteria:

1. a clearly defined region of high OSI (>0.1) around the aneurysm neck, with the OSI in the dome remaining lower than that near the neck;
2. a homogeneous transition from the high-OSI region to the lower-OSI region, with no additional local maxima;
3. an OSI ratio of at least 5 between the high-OSI region near the neck and the dome.

Although commonly observed in smaller aneurysms (e.g., Figure 2.a.), it is not restricted solely to them. In contrast, an aneurysm lacking an AOB, as depicted in Figure 3, exhibits a more heterogeneous distribution of both high and low OSI regions.

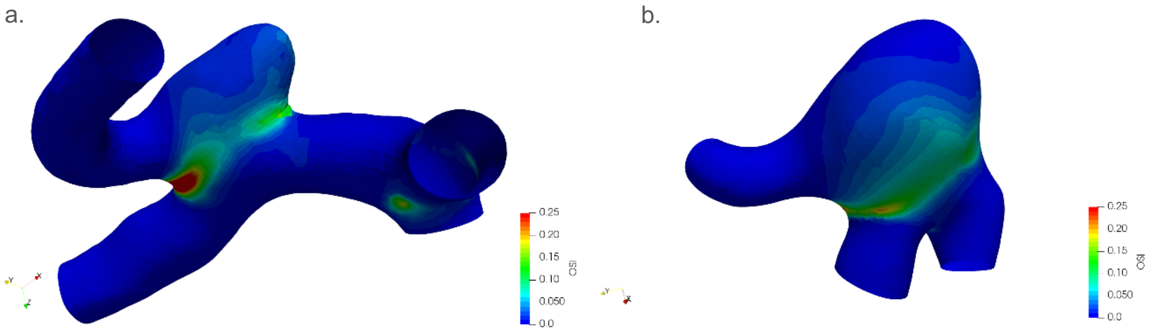

Figure 2. Oscillatory shear index (OSI) with visible AOB around aneurysm neck and homogeneous low distribution of OSI across the dome with size of 4.7 mm (a); AOB on exemplary aneurysm with size of 7.6 mm (b).

2.5 Wall thickness estimation

In this work, a constant wall thickness of 0.2 mm is utilized based on [25] and [30]. Currently, it is not possible to derive wall thickness of cerebral blood vessels from patient image data. Only via operative images is it possible to qualitatively estimate the location of thin-walled and thick-walled regions on the aneurysm surface. Thus, it is desirable to find a workflow, which can estimate the wall thickness distribution for subsequent non-constant wall simulations based on constant wall thickness simulations.

The following analysis method was utilized in our study:

- Pre-processing stage
    - A detailed analysis of intraoperative images from all 25 aneurysms was conducted identifying thin or thick regions (as suggested by Furukawa et al. [8]) by three separate individuals.
    - Based on the identified regions two representative evaluation points were defined in each thin as well as thick regions per aneurysm (see red dots for thin region and yellow dots in thick region on example aneurysm in Figure 3, as suggested by Furukawa et al. [8]).
- Simulation stage
    - Patient data of all 25 aneurysms as described in Section 2.1 were converted to simulation mesh.
    - FSI simulations are run for all aneurysms as described by equations 1-7.
    - Simulation results are written out for post-processing stage.
- Post-processing stage
    - The representative evaluation locations defined during pre-processing are utilized for the evaluation of fluid dynamic WSS, OSI as well as structural mechanical MISES and ES from simulations.
    - These hemodynamic and structural mechanical parameters are extracted for all representative points in all aneurysms and sorted by thin and thick regions.
    - Statistical analyses are performed between these data sets with Mann-Whitney U-tests to determine p-values (<0.05) for statistical significance between thin and thick wall thicknesses (for WSS, OSI, MISES and ES). In addition, box plots are generated of data in thick regions and thin regions in aneurysms (Figure 4 and Table 4.)

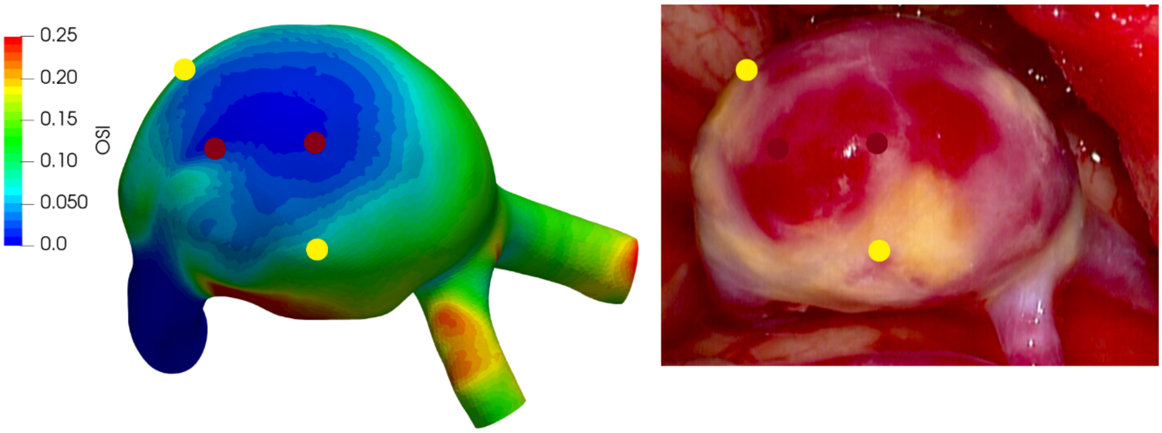

Figure 3. Simulation of an aneurysm geometry color-coded by the Oscillatory Shear Index (left), where no AOB is observable. The corresponding intraoperative image (right) shows yellow markers at thick-walled regions and red markers at thin-walled regions, following the convention described by Furukawa et al. [8].

In order to estimate the influence of the wall thickness of 0.2mm on the OSI and with it our interpretation of results, we conduct a wall thickness study with 0.3 and 0.4 mm.

2.6 Grouping of patients

To evaluate the statistical impact of the AOB, two cohorts were established:

1. Cohort #1: Included all 25 aneurysms without any exclusions. Among these, 15 aneurysms exhibited thick-walled regions, and 24 showed thin-walled regions.
2. Cohort #2: Excluded nine aneurysms with a significantly developed AOB (Figure 2), reducing the sample to 16 aneurysms. Within this subgroup, 12 aneurysms had thick-walled regions, and 15 had thin-walled regions.

U-tests as well as box plots (as explained in Section 2.5 were generated for both cohorts.

3 Results

This section contains the results of our numerical study on residual methods as well as medical implementation of the FSI simulations.

3.1 Influence of residual methods

Table 2 shows the performance of residual approaches 1 and 2 as presented before. For this performance evaluation both methods were utilized with a maximum allowed FSI iteration step of 3, 4, 5, 6, 7, 8, 9 and 10. Evaluation of results in Table 2 are not evaluated on selected evaluation points (as described above and as conducted in the analysis below), but rather averaged over entire aneurysm surface (including both thin and thick walled regions). This is since here we want to evaluate the influence of residual methods on the behaviour of the entire aneurysm surface instead of the individual thickness regions.

Residual method 1 exhibits variations in average parameters when the number of maximum allowed FSI iterations is below the maximum limit of 8, indicating that the system has not yet fully converged within a single time step. Once the number of iterations exceeds 8, the average values stabilize, suggesting convergence. Conversely, Residual method 2 shows parameter changes for maximum allowed FSI iteration counts below 5, but the results remain consistent and do not change beyond this point. This indicates a significant improvement in simulation runtime without any loss in results quality.

3.2 Clinical parameters

Table 3 provides a summary of the clinical data for the patients included. The average age was 56.44 years, with 12 male and 13 female patients. Thirteen patients had hypertension, while only four were smokers.

3.3 Morphological parameters

An AOB was detected in 9 patients. Since cohorts do not show normal distribution a Mann-Whitney U-test was conducted to analyze the statistical differences.

The morphological differences between aneurysms with and without an AOB were not statistically significant ($p > 0.05$). In addition, a separate analysis comparing Cohort 1 (aneurysms with and without an AOB) to Cohort 2 (aneurysms without an AOB) did not reveal any statistically significant differences in mean morphological parameters (see Table 4).

3.4 Hemodynamic and structural mechanical parameters

Hemodynamic parameters—WSS and OSI—as well as structural mechanical measures—equivalent strain (ES) and equivalent stress (MISES)—were evaluated at given evaluation points in thin-walled and thick-walled regions (where available) for each of the 25 aneurysms (see Figure 3 for representative evaluation points). The box plots of these parameters, along with their corresponding Mann–Whitney U-test p-values for thin versus thick regions, are summarized in Figure 4.

Cohort 1 comprised all 25 aneurysms, and no significant differences were observed between thin- and thick-walled regions for any of the parameters examined. In Cohort 2 ($n = 16$), which excluded aneurysms displaying an AOB, OSI—but not WSS—was significantly lower in thin-walled areas compared to thick-walled areas. Structural mechanical parameters did not differ significantly in either cohort.

Results above are shown for wall thickness of 0.2 mm based on [25,30]. In order to estimate the influence of the wall thickness we evaluate the values of WSS, OSI, MISES and ES at increased wall thickness values of 0.3 and 0.4 mm. Table 5 shows the influence of changed thickness.

On the structural mechanical side, since the aneurysm is a thin-walled structure, we utilize a linear elastic material model and we do not change the pressure profile, stress is inversely proportional to the wall thickness, thus a thickness of 0.3 mm lowers the stress by a factor of ~0.67 in simulations and a thickness of 0.4 mm lowers it by a factor of ~0.5. As the strain has a linear proportionality the same factors can be seen in the strain results as well.

Due to the fact, that strain values change in a low range (average values all < 0.03), the fluid volume does not change considerably in the process and WSS and OSI are only slightly changed (WSS by < 6%; OSI by < 4%) in the cases with increased wall thickness.

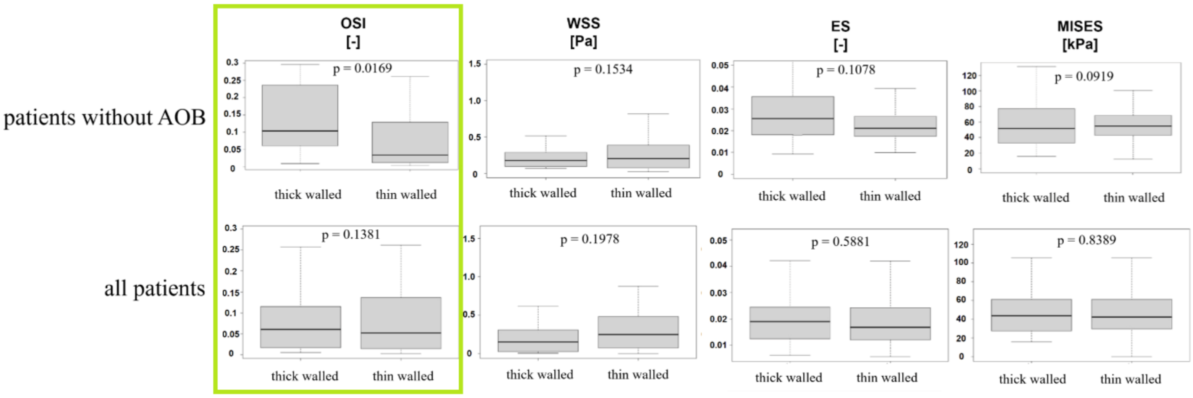

Figure 4. Box plots of WSS, OSI, ES and MISES; cohort #2 (top row); cohort #1 (bottom row); p-values in Mann-Whitney U-test comparing the thin and thick regions.

4 Discussion

In this study, we investigated FSI-simulations with morphological and hemodynamic analyses to evaluate the role of the AOB in assessing wall thickness in MCA-aneurysms. The investigation into FSI coupling methods revealed a notable enhancement in computational efficiency through the implementation of a novel residual method. As evidenced by the stabilization of average parameter values with fewer iterations and a reduced simulation runtime, Residual method 2 demonstrates a faster convergence rate compared to the default Residual method 1. This improvement is significant, as it suggests a substantial reduction in computational cost without compromising the accuracy of hemodynamic and structural mechanical parameters. The findings indicate that by comparing the absolute spatial coordinates of the fluid and solid interfaces, residual method #2 achieves a more efficient and stable FSI coupling in soft tissues, offering a valuable approach for future simulations requiring high computational demands.

This work also constitutes a comparison of AOB based OSI calculations with intraoperative images, providing confirmation that computational predictions can reflect actual wall characteristics. With the help of the novel metric AOB aneurysms can be excluded from investigation, where no relationship between OSI and wall thickness can be made. With this the focus can be put onto aneurysms, where wall thick estimation is possible with the help of calculated OSI distribution with constant wall thickness.

Recent research has increasingly focused on the influence of WSS and OSI in differentiating ruptured from unruptured aneurysms [40–43], and Meng et al. proposed that these hemodynamic factors may contribute to aneurysm formation and progression [44]. More advanced approaches now incorporate FSI modelling to account for the mechanical properties of the vessel wall [25,26,33], offering a more comprehensive view of how local hemodynamics intersect with structural integrity [25,26]. A possible future utilization of the OSI based wall thickness estimation may be improved FSI simulations, where wall thickness can be estimated without intraoperative images.

Beyond risk stratification, such detailed aneurysm wall characterization carries significant implications for neurosurgical planning. Different wall morphologies demand distinct intraoperative strategies; thick, calcified regions complicate clip placement, whereas thin-walled areas are prone to rupture [6–10]. Several studies have attempted to identify thick versus thin regions from hemodynamic data, but findings have been inconsistent [8,9,11–15]. Potential causes include subjectivity in wall-thickness classification from intraoperative images [8,9,11–15], variability in anatomical locations [8,12,21], and the inclusion of both ruptured and unruptured aneurysms [15]. Karnam et al. demonstrated distinct hemodynamic patterns in blebs of anterior communicating artery and MCA aneurysms [45]. By focusing solely on unruptured MCA aneurysms, our study reduces anatomical variability.

Cebral et al. observed that hyperplastic and atherosclerotic regions exhibit higher OSI values compared to thin-walled areas [12], aligning with our findings. Similarly, Cho et al. found OSI predictive of thin-walled areas [21]. However, some studies reported no significant differences [23,24], and Veeturi et al. noted elevated WSS but not OSI in thin regions [22]. These discrepancies underscore the complexity of aneurysm hemodynamics and highlight the need for robust analytical methods.

We introduce the AOB as a novel stratification strategy based on OSI patterns. In aneurysms with a well-defined AOB, OSI is uniformly elevated near the neck, with lower OSI in the dome. In contrast, aneurysms lacking an AOB exhibit more heterogeneous OSI distributions. By excluding AOB-positive aneurysms, our analysis demonstrates that only aneurysms with heterogeneous OSI show a statistically significant difference in OSI between thin- and thick-walled regions. Neither WSS nor structural mechanical parameters—equivalent wall stress (MISES) or equivalent wall strain (ES)—differed, and morphological parameters likewise failed to achieve significance. These results suggest that AOB operates independently of established morphological factors such as size or aspect ratio [1]. Notably, identifying thin regions through a heterogeneous OSI distribution underscores OSI's potential as a valuable preoperative indicator of weak aneurysm zones.

5 Limitations

Despite these promising findings, certain limitations must be noted. First, assumptions regarding the artery's baseline geometry were necessary during aneurysm segmentation, reflecting current imaging resolution constraints. Moreover, the simulations did not incorporate potential interactions with surrounding brain tissue, which may influence aneurysm behavior in vivo.

A uniform vessel wall thickness of 0.2 mm was employed based on existing literature [25,30], which may introduce variability into the analysis. However, this simplification reflects a realistic clinical scenario in which neurosurgeons typically do not have access to precise preoperative thickness measurements. By utilizing the approach proposed herein, future studies will be able to address and circumvent this limitation. Given that strain values remained low (< 0.05), the overall hemodynamic outcomes are unlikely to be severely impacted by minor wall deformations. Finally, the absence of patient-specific material properties (e.g., Young's modulus, Poisson's ratio) necessitated certain assumptions, limiting the absolute precision of the models. A wall thickness study showed that hemodynamic quantities are not significantly changed by the thickness of the wall, thus our interpretation of OSI results are independent from the quantitative value of the initially assumed constant thickness of the wall. From the OSI distribution in future simulations it will be potentially possible to derive a vessel wall with non-constant thickness, thus improving the quality of FSI simulations.

A further limitation of this study is the relatively small sample size of 25 patients, which may limit the generalizability of the findings. While the results demonstrate promising correlations between the AOB, OSI, and aneurysm wall characteristics within this cohort, a larger patient population is needed to confirm these observations and reduce the potential for statistical bias. To address this limitation, the authors are planning a multicenter study to validate these findings in a more diverse and representative cohort, thereby strengthening the clinical relevance and applicability of the proposed methodology.

6 Conclusions

This study underscores the importance of integrating hemodynamic and structural mechanical parameters to estimate wall thickness in MCA aneurysms. By introducing the "aneurysm-OSI-band", we propose a stratification mechanism that leverages OSI as a key indicator. Specifically, aneurysms with heterogeneous OSI distributions exhibited a clear statistical distinction between thin- and thick-walled regions. We present a comparison of AOB based calculations with intraoperative images, showing agreement and validating the clinical potential of this computational approach. Moving forward, multicenter and prospective studies are planned to confirm these findings and further refine OSI-based patient stratification.

7 Acknowledgement

This work was supported by a grant from Medical Society of Upper Austria MedGes OÖ (Medizinische Gesellschaft für Oberösterreich) as well as research subsidies granted by the government of Upper Austria via the FFG (Austrian Research Promotion Agency) [grant number FO999895610 (Project ARES)]. RISC Software GmbH is Member of UAR (Upper Austrian Research) Innovation Network.

8 Ethical considerations

This study was approved by the local ethics committee (Ethikkommission der medizinischen Fakultät der Johannes Kepler Universität; EK Nr: 1129/2022). All procedures performed were in accordance with the ethical standards of the institutional and national research committee, and with the 1964 Helsinki Declaration and its later amendments or comparable ethical standards.

Informed consent from patients was waived owing to the retrospective nature of the research. The need to obtain informed consent was waived by the Ethikkommission der medizinischen Fakultät der Johannes Kepler Universität: 1129/2022.

9 Data Availability Statement

The data are not publicly available due to the fact that authors want to keep patient data private, however data can be made available upon request.

10 Nomenclature

Units are provided where applicable.

Abbreviations:

AOB	Aneurysm-OSI-Band
AR	Aspect Ratio
CFD	Computational Fluid Dynamics
DSA	Digital Subtraction Angiography
EI	Ellipticity Index [-]
ES	Equivalent Strain
FSI	Fluid-Structure Interaction
MCA	Middle Cerebral Artery
MISES	Equivalent Stress [MPa]
OSI	Oscillatory Shear Index [-]
SAH	Subarachnoid Hemorrhage
S	Size [mm]
SR	Size Ratio [-]
WSS	Wall Shear Stress [Pa]

Variables:

	Wall Shear Stress [Pa]
$\boldsymbol{n_o}$	Unit normal vector
	Effective viscosity [Pa s]
$\boldsymbol{u}$	Fluid velocity [m/s]
p	Pressure [Pa]
ρ	Fluid density [kg/m^3]
ρ_o	Solid density [kg/m^3]
τ	Fluid stress tensor
$\boldsymbol{D}$	Solid displacement [m]
σ_s	Solid stress [Pa]
$\boldsymbol{b}$	Solid body force
μ	Shear modulus
λ	First Lamé parameter
E	Young’s modulus [MPa]
ν	Poisson’s ratio [-]
$\Delta\boldsymbol{d}_i^s$	Displacement increment of the solid interface
$\Delta\boldsymbol{d}_i^f$	Displacement increment of the fluid interface

$\boldsymbol{R}_i$	Residual at the i-th FSI iteration
x_i^f	Position vector in fluid
x_i^s	Position vector in solid
t	Time [s]

11 References

[1] S. Dhar, M. Tremmel, J. Mocco, M. Kim, J. Yamamoto, A. H. Siddiqui, “Morphology parameters for aneurysm rupture risk assessment,” in Neurosurgery, 2008, vol. 63, no. 2, pp. 185–197, doi: https://doi.org/10.1227/01.NEU.0000316847.64140.81.

[2] S. Jirjees, Z. M. Htun, I. Aldawudi, P. C. Patwal, S. Khan, “Role of morphological and hemodynamic factors in predicting intracranial aneurysm rupture: a review,” in Cureus, 2020, vol. 12, no. 7, e9178, doi: https://doi.org/10.7759/cureus.9178.

[3] H. Meng, V. M. Tutino, J. Xiang, A. Siddiqui, “High WSS or low WSS? Complex interactions of hemodynamics with intracranial aneurysm initiation, growth, and rupture: toward a unifying hypothesis,” in AJNR Am J Neuroradiol, 2014, vol. 35, no. 7, pp. 1254–1262, doi: https://doi.org/10.3174/ajnr.A3558.

[4] A. Morita, T. Kirino, K. Hashi, N. Aoki, S. Fukuhara, N. Hashimoto, T. Nakayama, et al., “The natural course of unruptured cerebral aneurysms in a Japanese cohort,” in N Engl J Med, 2012, vol. 366, pp. 2474–2482, doi: https://doi.org/10.1056/NEJMoa1113260.

[5] K. A. M. Hackenberg, D. Hänggi, N. Etminan, “Unruptured intracranial aneurysms,” in Stroke, 2018, vol. 49, no. 9, pp. 2268–2275, doi: https://doi.org/10.1161/STROKEAHA.118.021030.

[6] S. Inci, A. Akbay, M. Orunoglu, “Aneurysm clip compression technique in the surgery of aneurysms with hard/calcified neck,” in World Neurosurgery, 2015, vol. 84, no. 3, pp. 688–696, doi: https://doi.org/10.1016/j.wneu.2015.04.039.

[7] R. Rahmani, J. F. Baranoski, F. C. Albuquerque, M. T. Lawton, T. Hashimoto, “Intracranial aneurysm calcification – a narrative review,” in Exp Neurol, 2022, vol. 353, 114052, doi: https://doi.org/10.1016/j.expneurol.2022.114052.

[8] K. Furukawa, F. Ishida, M. Tsuji, Y. Miura, T. Kishimoto, M. Shiba, et al., “Hemodynamic characteristics of hyperplastic remodeling lesions in cerebral aneurysms,” in PLoS One, 2018, vol. 13, no. 1, e0191287, doi: https://doi.org/10.1371/journal.pone.0191287.

[9] H. Kimura, M. Taniguchi, K. Hayashi, Y. Fujimoto, Y. Fujita, T. Sasayama, et al., “Clear detection of thin-walled regions in unruptured cerebral aneurysms by using computational fluid dynamics,” in World Neurosurgery, 2019, vol. 121, pp. e287–e295, doi: https://doi.org/10.1016/j.wneu.2018.09.098.

[10] Y. Chen, B. Lin, J. Zhou, L. Chen, Y. Yang, B. Zhao, “Morphological predictors of middle cerebral artery bifurcation aneurysm rupture,” in Clin Neurol Neurosurg, 2020, vol. 192, p. 105708, doi: https://doi.org/10.1016/j.clineuro.2020.105708.

[11] A. S. F. S. Ashkezari, F. J. Detmer, F. Mut, B. J. Chung, A. K. Yu, C. J. Stapleton, et al., “Bleb in intracranial aneurysms: prevalence and general characteristics,” in J Neurointerv Surg, 2021, vol. 13, no. 3, pp. 226–230, doi: https://doi.org/10.1136/neurintsurg-2020-016274.

[12] J. R. Cebral, F. Detmer, B. J. Chung, J. Choque-Velasquez, B. Rezai, H. Lehto, et al., “Local hemodynamic conditions associated with focal changes in the intracranial aneurysm wall,” in AJNR Am J Neuroradiol, 2019, vol. 40, no. 3, pp. 510–516, doi: https://doi.org/10.3174/ajnr.A5970.

[13] P. Jiang, Q. Liu, J. Wu, X. Chen, M. Li, Z. Li, et al., “Hemodynamic characteristics associated with thinner regions of intracranial aneurysm wall,” in J Clin Neurosci, 2019, vol. 67, pp. 185–190, doi: https://doi.org/10.1016/j.jocn.2019.06.024.

[14] L. M. Kadasi, W. C. Dent, A. M. Malek, “Colocalization of thin-walled dome regions with low hemodynamic wall shear stress in unruptured cerebral aneurysms,” in J Neurosurg, 2013, vol. 119, no. 1, pp. 172–179, doi: https://doi.org/10.3171/2013.2.JNS12968.

[15] T. Suzuki, C. J. Stapleton, M. J. Koch, K. Tanaka, S. Fujimura, T. Suzuki, et al., “Decreased wall shear stress at high-pressure areas predicts the rupture point in ruptured intracranial aneurysms,” in J Neurosurg, 2019, vol. 132, no. 4, pp. 1116–1122, doi: https://doi.org/10.3171/2018.12.JNS182897.

[16] S. Omodaka, S. Sugiyama, T. Inoue, K. Funamoto, M. Fujimura, H. Shimizu, et al., “Local hemodynamics at the rupture point of cerebral aneurysms determined by computational fluid dynamics analysis,” in Cerebrovasc Dis, 2012, vol. 34, pp. 121–129, doi: https://doi.org/10.1159/000339678.

[17] K. Fukazawa, F. Ishida, Y. Umeda, Y. Miura, S. Shimosaka, S. Matsushima, et al., “Using computational fluid dynamics analysis to characterize local hemodynamic features of middle cerebral artery aneurysm rupture points,” in World Neurosurg, 2015, vol. 83, pp. 80–86, doi: https://doi.org/10.1016/j.wneu.2013.02.012.

[18] S. Sugiyama, K. Niizuma, T. Nakayama, H. Shimizu, H. Endo, T. Inoue, et al., “Relative residence time prolongation in intracranial aneurysms: a possible association with atherosclerosis,” in Neurosurgery, 2013, vol. 73, pp. 767–776, doi: https://doi.org/10.1227/NEU.0000000000000096.

[19] S. S. Sugiyama, H. Endo, K. Niizuma, T. Endo, K. Funamoto, M. Ohta, et al., “Computational hemodynamic analysis for the diagnosis of atherosclerotic changes in intracranial aneurysms: a proof-of-concept study using 3 cases harboring atherosclerotic and nonatherosclerotic aneurysms simultaneously,” in Comput Math Methods Med, 2016, 2016, 2386031, doi: https://doi.org/10.1007/s00234-021-02803-x.

[20] S. Talari, Y. Kato, H. Shang, Y. Yamada, K. Yamashiro, D. Suyama, et al., “Comparison of computational fluid dynamics findings with intraoperative microscopy findings in unruptured intracranial aneurysms: an initial analysis,” in Asian J Neurosurg. 2016 Oct-Dec;11(4):356-360. doi: https://doi.org/10.4103/1793-5482.180962.

[21] C. K. Cho, J. H. Choi, J. H. Oh, Y. B. Kim, “Prediction of thin-walled areas of unruptured cerebral aneurysms through comparison of normalized hemodynamic parameters and intraoperative images,” in Biomed Res Int, 2018, Art. no. 3047181, doi: https://doi.org/10.1155/2018/3047181.

[22] S. S. Veeturi, T. R. Patel, A. A. Baig, A. Chien, A. Monteiro, M. Waqas, et al., “Hemodynamic analysis shows high wall shear stress is associated with intraoperatively observed thin wall regions of intracranial aneurysms,” in J Cardiovasc Dev Dis, 2022, vol. 9, no. 12, Art. no. 424, doi: https://doi.org/10.3390/jcdd9120424.

[23] P. Jiang, Q. Liu, J. Wu, X. Chen, M. Li, Z. Li, et al., “Hemodynamic characteristics associated with thinner regions of intracranial aneurysm wall,” in J Clin Neurosci, 2019, vol. 67, pp. 185–190, doi: https://doi.org/10.1016/j.jocn.2019.06.024.

[24] P. Jiang, Q. Liu, J. Wu, X. Chen, M. Li, F. Yang, et al., “Hemodynamic findings associated with intraoperative appearances of intracranial aneurysms,” in Neurosurg Rev, 2020, vol. 43, no. 1, pp. 203–209, doi: https://doi.org/10.1007/s10143-018-1027-0.

[25] C. K. Cho, H. Yang, J. J. Kim, J. H. Oh, Y. B. Kim, “Prediction of rupture risk in cerebral aneurysms by comparing clinical cases with fluid-structure interaction analyses,” in Sci Rep, 2020, vol. 10, Art. no. 18237, doi: https://doi.org/10.1038/s41598-020-75362-5.

[26] H. Yang, C. K. Cho, J. J. Kim, J. H. Kim, Y. B. Kim, J. H. Oh, “Rupture risk prediction of cerebral aneurysms using a novel convolutional neural network-based deep learning model,” in J Neurointerv Surg, 2023, vol. 15, no. 2, pp. 200–204, doi: https://doi.org/10.1136/neurintsurg-2021-018551.

[27] J. R. Cebral, F. Detmer, B. J. Chung, J. Choque-Velasquez, B. Rezai, H. Lehto, et al., “Local hemodynamic conditions associated with focal changes in the intracranial aneurysm wall,” in AJNR Am J Neuroradiol, 2019, vol. 40, no. 3, pp. 510–516, doi: https://doi.org/10.3174/ajnr.A5970.

[28] L. M. Kadasi, W. C. Dent, A. M. Malek, “Cerebral aneurysm wall thickness analysis using intraoperative microscopy: effect of size and gender on thin translucent regions,” in J Neurointerv Surg, 2013, vol. 5, no. 3, pp. 201–206, doi: https://doi.org/10.1136/neurintsurg-2012-010285.

[29] L. M. Kadasi, W. C. Dent, A. M. Malek, “Colocalization of thin-walled dome regions with low hemodynamic wall shear stress in unruptured cerebral aneurysms: clinical article,” in J Neurosurg, 2013, vol. 119, no. 1, pp. 172–179, doi: https://doi.org/10.3171/2013.2.JNS12968.

[30] J. M. Acosta, A. F. Cayron, N. Dupuy, G. Pelli, B. Foglia, J. Haemmerli, et al., “Effect of aneurysm and patient characteristics on intracranial aneurysm wall thickness,” in Front Cardiovasc Med, 2021, vol. 8, Art. no. 775307, doi: https://doi.org/10.3389/fcvm.2021.775307.

[31] H. G. Weller, G. Tabor, H. Jasak, C. Fureby, “A tensorial approach to computational continuum mechanics using object-oriented techniques,” in Comput Phys, 1998, vol. 12, no. 6, pp. 620–631, doi: https://doi.org/10.1063/1.168744.

[32] P. Cardiff, A. Karač, P. De Jaeger, H. Jasak, J. Nagy, A. Ivanković, Ž. Tuković, “An open-source finite volume toolbox for solid mechanics and fluid-solid interaction simulations,” arXiv, 2018, arXiv:1808.10736v2. Available: https://arxiv.org/abs/1808.10736.

[33] J. Nagy, W. Fenz, V. M. Miron, S. Thumfart, J. Maier, Z. Major, et al., “Fluid-structure interaction simulations of the initiation process of cerebral aneurysms,” in Brain Sci, 2024, vol. 14, p. 977, doi: https://doi.org/10.3390/brainsci14100977.

[34] J. Nagy, J. Maier, V. Miron, W. Fenz, Z. Major, et al., “Methods, validation, and clinical implementation of a simulation method for cerebral aneurysms,” in JBEB, 2023, vol. 10, pp. 10–19, doi: https://doi.org/10.11159/jbeb.2023.003.

[35] J. Nagy, W. Fenz, S. Thumfart, J. Maier, Z. Major, H. Stefanits, et al., “Fluid structure interaction analysis for rupture risk assessment in patients with middle cerebral artery aneurysms,” in Sci Rep, 2025, Jan 14, vol. 15, no. 1, p. 1965, doi: https://doi.org/10.1038/s41598-024-85066-9.

[36] F. Lorenzetti, S. Suominen, E. Tukianen, “Evaluation of blood flow in free microvascular flaps,” in J Reconstr Microsurg Open, 2001, vol. 17, no. 3, pp. 163–167, doi: https://doi.org/10.1055/s-2001-14347.

[37] P. Blanco, L. Müller, J. D. Spence, “Blood pressure gradients in cerebral arteries: a clue to pathogenesis of cerebral small vessel disease,” in Stroke Vasc Neurol, 2017, vol. 2, no. 3, pp. 108–117, doi: https://doi.org/10.1136/svn-2017-000087.

[38] B. K. Toth, “The mechanical interaction between the red blood cells and the blood vessels,” Ph.D. dissertation, University of Budapest, 2012.

[39] C. Reeps, M. Gee, A. Maier, M. Gurdan, H. H. Eckstein, W. Wall, “The impact of model assumptions on results of computational mechanics in abdominal aortic aneurysm,” in J Vasc Surg, 2010, vol. 51, pp. 679–688, doi: https://doi.org/10.1016/j.jvs.2009.10.048.

[40] P. Jiang, Q. Liu, J. Wu, X. Chen, M. Li, Z. Li, et al., “A novel scoring system for rupture risk stratification of intracranial aneurysms: a hemodynamic and morphological study,” in Front Neurosci, 2018, vol. 12, p. 596, doi: https://doi.org/10.3389/fnins.2018.00596.

[41] F. J. Detmer, B. J. Chung, F. Mut, M. Slawski, F. Hamzei-Sichani, C. Putman, et al., “Development and internal validation of an aneurysm rupture probability model based on patient characteristics and aneurysm location, morphology, and hemodynamics,” in Int J CARS, 2018, vol. 13, pp. 1767–1779, doi: https://doi.org/10.1007/s11548-018-1837-0.

[42] F. J. Detmer, B. J. Chung, F. Mut, M. Slawski, F. Hamzei-Sichani, C. Putman, et al., “Development of a statistical model for discrimination of rupture status in posterior communicating artery aneurysms,” in Acta Neurochir, 2018, vol. 160, pp. 1643–1652, doi: https://doi.org/10.1007/s00701-018-3595-8.

[43] J. Fan, Y. Wang, J. Liu, L. Jing, C. Wang, C. Li, et al., “Morphological-hemodynamic characteristics of intracranial bifurcation mirror aneurysms,” in World Neurosurg, 2015, vol. 84, no. 1, pp. 114–120, doi: https://doi.org/10.1016/j.wneu.2015.02.038.

[44] H. Meng, V. M. Tutino, J. Xiang, A. Siddiqui, “High WSS or low WSS? Complex interactions of hemodynamics with intracranial aneurysm initiation, growth, and rupture: toward a unifying hypothesis,” in AJNR Am J Neuroradiol, 2014, vol. 35, no. 7, pp. 1254–1262, doi: https://doi.org/10.3174/ajnr.A3558.

[45] Y. Karnam, F. Mut, A. K. Yu, B. Cheng, S. Hanjani, F. T. Charbel, et al., “Distribution of rupture sites and blebs on intracranial aneurysm walls suggests distinct rupture patterns in ACom and MCA aneurysms,” in Int J Numer Method Biomed Eng, 2024, vol. 40, no. 8, p. e3837, doi: https://doi.org/10.1002/cnm.3837.

12 Appendix

Table 1. Description and overview of hemodynamic, structural mechanical as well as morphological parameters.

Parameter type	Parameter	Description
Hemodynamic	Wall Shear Stress (WSS)	Magnitude of the viscous forces of the blood flow on the vessel wall - $\tau_w = \hat{n} \cdot \left(\mu(\nabla u + (\nabla u)^T)\right)$
	Oscillatory Shear Index (OSI)	Degree of directional oscillation of the WSS vector during the cardiac cycle - $OSI = \frac{1}{2}\left(1 - \frac{\left\lvert\int_0^T \tau_w(t)\,dt\right\rvert}{\int_0^T \lvert\tau_w(t)\rvert\,dt}\right)$
Structural mechanical	Equivalent strain (ES)	Equivalent relative deformation, compared to a reference position configuration
	Equivalent Stress (MISES)	Scalar stress value determining if a given material will yield or fracture, if above a material specific value
Morphological	Size (S)	Mean diameter of the aneurysm
	Aspect ratio (AR)	Mean diameter of the aneurysm
	Size ratio (SR)	Ratio of aneurysm size to parent vessel diameter
	Aneurysm angle (AA)	Angle measured between the vector connecting the center of the aneurysm's neck plane to the point on the aneurysm surface with the largest normal distance from this plane and the normal vector of the neck plane itself
	Ellipticity index (EI)	Measure of the elongation of the aneurysm

Table 2. Influence of residual methods on hemodynamic, structural mechanical parameters averaged in the entire aneurysm dome as well as average simulation runtime

Residual method	Number of FSI loops	WSS [Pa]	OSI [-]	ES [-]	MISES [kPa]	Runtime [s]
#1	3	0.078	0.153	0.023	69.1	470
	4	0.079	0.151	0.027	70.3	628
	5	0.080	0.150	0.029	70.8	784
	6	0.081	0.149	0.030	71.0	939
	7	0.082	0.148	0.031	71.2	1096
	8	0.082	0.148	0.032	71.3	1251
	9	0.082	0.148	0.032	71.3	1408
	10	0.082	0.148	0.032	71.3	1565
#2	3	0.081	0.149	0.030	70.9	472
	4	0.082	0.148	0.031	71.1	629
	5	0.082	0.148	0.032	71.3	786
	6	0.082	0.148	0.032	71.3	941
	7	0.082	0.148	0.032	71.3	1099
	8	0.082	0.148	0.032	71.3	1254
	9	0.082	0.148	0.032	71.3	1411
	10	0.082	0.148	0.032	71.3	1568

Table 3. Patient Demographics and Data Overview

Characteristic	Number of patients (n=25)	Percentage [%]
Patient age [y]	56.44±10.14	
Gender		
Male	12	48.0
Female	13	52.0
Hypertension		
Yes	13	52.0
No	12	48.0
Smoking		
Yes	4	16.0
No	21	84.0
Aneurysm size [mm]		
Mean ± SD	5.9±3.2	
Range	2.0-12.0	

Table 4. Mann–Whitney U-test p-values for morphological parameters in aneurysms with and without an AOB as well as all aneurysms and aneurysms without AOB.

Parameter	p-value between aneurysms with and without AOB	p-value between aneurysms in cohort 1 and cohort 2
Size	0.1468	0.1671
Aspect ratio	0.3685	0.3492
Size ratio	0.2757	0.2657
Aneurysm angle	0.8148	0.6919
Ellipticity index	0.7159	0.6468

Table 5. Influence of wall thickness on hemodynamic, structural mechanical parameters as in thick- and thin-walled regions (as identified in operative images) in evaluation points in aneurysms without OSI band.

thickness region in operative images	constant wall thickness [mm]	WSS [Pa]	OSI [-]	ES [-]	MISES [kPa]
thick	0.2	0.249	0.119	0.027	51.5
	0.3	0.254	0.117	0.018	34.6
	0.4	0.264	0.115	0.014	25.9
thin	0.2	0.270	0.055	0.020	54.2
	0.3	0.275	0.054	0.013	36.2
	0.4	0.286	0.053	0.010	27.2